OFDM-based Spatial Data Focusing for Wireless Physical Layer Geocasting in Multipath Channels

Guylian Molineaux, *Student Member, IEEE,* François Horlin, *Member, IEEE,*
Philippe De Doncker, *Member, IEEE,* Julien Sarrazin, *Senior Member, IEEE*

Abstract—**OFDM-based spatial data focusing (OFDM-SDF) is proposed as a novel means of performing wireless physical layer geocasting, i.e. spatially confined broadcasting. It is shown that this approach overcomes beamforming and directional modulation (DM) limitations by exhibiting higher spatial precision with a reduced number of antennas and offering uncoupled range-angle-dependent focusing. This paper describes the OFDM-SDF system model for multipath channels, including multipath robust equalization, design rules for steering phases and sidelobe mitigation, analytical geocast delivery zone derivation, and optimized symbol mapping. Using density-based clustering of the spatial bit error rate distribution, a procedure for identifying a practical geocast delivery zone and evaluating its precision and connectivity is proposed. OFDM-SDF's performance and multipath robustness are evaluated through Rice channel simulations as a function of the Rice factor. In particular, it is shown that a 2-antenna OFDM-SDF array matches the radial and angular precision of, respectively, a 6 and 12-antenna DM array in recent literature, while robustness is ensured for 5G small cell channels.**

Index Terms—**Geocasting, spatial data focusing (SDF), mobile ad hoc networks (MANETs), subcarrier selection, DBSCAN.**

I. Introduction

GEOCASTING, or location-based multicasting, is the spatially confined broadcasting of information, targeting exclusive delivery to users within restricted geographical regions. It allows to offer location-dependent services and messaging to large groups of mobile devices that exist in the context of Internet-of-Things, Smart Cities, and Wireless Sensor Networks, e.g. for advertising and marketing, traffic management, emergency signaling, tourism, etc. [1], [2]. Additionally, as it targets a physical area, rather than the individual users that may or may not reside in it, geocasting does not require centralized knowledge of a node's physical location, thus respecting user privacy and avoiding delays associated to the exchange of such information.

By integrating the concept of physical position into the logical addressing of networks, geocasting can be achieved through geographic or location-based routing protocols [3]. Many of these algorithms struggle however to balance delivery rate, overhead, and scalability in dynamic mobile ad hoc networks (MANETs) of varying densities [4], [5]. Additionally, they rely on a cooperative node's ability to determine its own position – often with respect to a positioning system that is limited in resolution, especially indoors, and that requires embedded receivers with high power consumption. Alternatively, geocast information can be (geographically) routed through a fixed network of base stations that forward information to all nodes within their coverage. This omits the aforementioned complexities inherent to multi-hop forwarding in MANETs and shifts the geocast burden from the network layer to the physical layer. Geocasting precision is then limited by the spatial selectivity of base stations and can be increased by equipping them with spatial focusing techniques. The resulting geocast delivery zone is given by the geographical region where the bit error rate (BER) is sufficiently low to allow reliable data retrieval.

Beamforming performs spatial power focusing by exploiting constructive and destructive interference between correlated signals transmitted from different elements in an array [6]. Geocasting is obtained through the location-dependent signal-to-noise ratio (SNR) that results from the directive array radiation pattern and impacts the BER accordingly. While classical phased arrays suffer from the constraint that focusing is limited to the angular dimension only, frequency diverse arrays (FDAs) have shown the ability for range-angle-dependent beamforming [7]. However, their beampatterns are continuous and coupled in the range and angular domains, such that no bounded geocast area can be obtained. Decoupling of range and angular focusing is feasible by using non-uniform frequency offsets in the array, e.g. using a random frequency diverse array (RFDA) [8], logarithmic FDA [9], or window-based FDA [10]. Being developed for radar applications, these schemes suffer from drawbacks in geocasting context, like stochastic beampattern description [8] and kilometer-range operation [9], [10]. More importantly, they fail to improve on the principal limitation of beamforming for geocasting, i.e. the requirement of large physical arrays to obtain narrow beams and high precision.

Directional modulation (DM) emerged originally as a means of securing beamforming against eavesdroppers in

sidelobe directions, where elevated SNR potentially results in undesired information leakage outside the intended area, hence providing a beneficial improvement in wireless geocasting context. Implemented either through pattern-reconfigurable arrays [11], [12] or excitation-reconfigurable arrays [13], [14], they fail however to provide considerable beamwidth improvements such that they remain limited in precision for geocasting, just as beamforming. Ultra-wideband pulse-based DM implementations [15], on the other hand, have shown significant beamwidth improvements using a minimal number of antennas. Wide inter-antenna separation prohibits however substantial reduction of the physical array size. Additionally, the single carrier nature of all above schemes limits them to angular focusing only.

More recent implementations have explored range-angle-dependent DM through FDAs [16], RFDAs [17], or random-subcarrier-selection [18], combined with artificial noise injection to enhance secrecy performance. Notably for geocasting, [19] investigates the spatial properties of the RFDA-DM secrecy zone. However, [16]–[19] are limited to single user scenarios, no longer satisfying the broadcasting aspect of geocasting. Multi-user broadcasting for DM has been achieved, first in the angular-domain [20] and later the range-angle-domain [21], [22]. However, a user-based rather than location-based service is provided. Indeed, design of the precoding vector requires individual targeting and localization of each user, complicating the simultaneous transmission to large groups of devices as well as voiding geocasting's user privacy prospects. Moreover, recent work [23] has shown that FDA and its variants suffer from time-variant beampatterns, such that the aforementioned techniques cannot confine their broadcasting to the same location in range as time elapses.

In contrast to beamforming and DM, spatial data focusing (SDF) attempts to address the geocasting issue directly, aiming for increased precision, reduced array size, and minimal complexity [24]. It abandons DM's and beamforming's power focusing approach, no longer basing signal distortion on array radiation pattern manipulation and the resulting spatial SNR distribution. Instead, it adopts the idea of channel-based modulation through the distributed transmission of information. Specifically, uncorrelated and orthogonal signals, carrying substreams of a global datastream, are transmitted over the sub-channels in a multiple-input single-output (MISO) setup. At the receiver, differences in propagation conditions between each data substream are exploited upon equalization to induce a location-dependent symbol distortion that restricts the spatial availability of the transmitted data, regardless of received power and SNR.

Time-based spatial data focusing (T-SDF), introduced in [24] and [25], exploits the temporal dimension for signal orthogonality. Despite the considerable increase in spatial selectivity over beamforming in the angular domain, T-SDF fails to achieve range-based focusing.

Alternatively, signal orthogonality can be obtained in the frequency domain by exploiting OFDM subcarrier orthogonality, i.e. OFDM-based spatial data focusing (OFDM-SDF). The supplementary multi-frequency degree
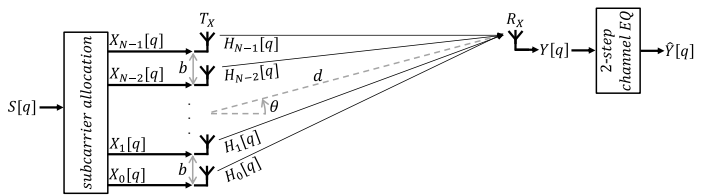

Fig. 1. Frequency domain OFDM-based spatial data focusing system model

of freedom that is so introduced can be leveraged to induce range-angle-dependent SDF. Note that in SDF, and by extension OFDM-SDF, transmitted signals are orthogonal, uncorrelated and separately processed at the receiver, hence not enforcing or exploiting the FDA beamforming radiation patterns proven time-variant by [23]. Similarly to [26], OFDM-SDF range focusing thus remains time-invariant.

Preliminary results on OFDM-SDF have been presented in [27]. However, just like [24] and [25], it is limited by omitting a multipath channel analysis and does not provide any performance guarantee in those scenarios. On the other hand, this paper presents an expanded OFDM-SDF scheme that allows for the dual exploitation of OFDM multi-frequency transmission for high-precision uncoupled range-angle-dependent and multipath robust geocasting. Additionally, an approach for practical geocast delivery zone identification and characterization is proposed using density-based clustering of the spatial BER distribution, together with performance metrics for precision and connectivity quantification. They are employed in a thorough simulation-based analysis that demonstrates OFDM-SDF's improved precision, flexibility, and multipath robustness for geocasting.

Section II presents the OFDM-SDF system model, including multipath robust equalization, design rules for steering phases and sidelobe mitigation, and analytic geocast delivery zone derivation. Practical delivery zone identification and evaluation are described in Section III and applied on simulation results in Section IV. Finally, conclusions are drawn in Section V.

II. SYSTEM MODEL

Fig. 1 shows the frequency domain system model that is used for OFDM-SDF. The transmitter employs a uniform linear array of N antennas with a spacing of b. Antennas are indexed by $n = 0, 1, \ldots, N - 1$, such that their position along the array axis, with respect to the array center, is given by $(n - \frac{N-1}{2})b$. The receiver moves in a 2-dimensional plane around the transmitter. Its position is described by the polar coordinates (d, θ), respectively the radial distance to the array center and the azimuth angle with respect to the array broadside direction. Q OFDM subcarriers are used, with subcarrier bandwidth B_c and zero-centered indices $q \in \mathcal{Q} = \left\{ -\frac{Q}{2}, -\frac{Q}{2} + 1, \ldots, \frac{Q}{2} - 1 \right\}$. Their frequencies with respect to a carrier frequency f_c can be expressed as $f_q = f_c + qB_c$, yielding a total bandwidth $B = QB_c$.

A. Transmitter: OFDM-SDF Precoding

Starting from conventional OFDM symbol blocks S, OFDM-SDF exploits OFDM subcarrier orthogonality to al-

low for distributed transmission of information in S across the array, without inter-channel interference. To this end, a subset of subcarriers $\mathcal{Q}_n \subset \mathcal{Q}$ is allocated to each antenna, ensuring that they are exhaustive $\mathcal{Q} = \bigcup_{n=0}^{N-1} \mathcal{Q}_n$ and disjoint $\mathcal{Q}_n \cap \mathcal{Q}_{n'} = \emptyset, \forall n, n' = 0, \ldots, N-1, n \neq n'$. A unique OFDM-block X_n is then defined for each antenna n, such that it contains the original symbol $S[q]$ on the subcarriers $q \in \mathcal{Q}_n$ assigned to that antenna and zeroes elsewhere, i.e.

$$ X_n[q] = \begin{cases} S[q]e^{j\varphi_{n,q}^{steer}} & q \in \mathcal{Q}_n \\ 0 & q \in \mathcal{Q} \setminus \mathcal{Q}_n. \end{cases} \quad (1) $$

A steering phase $\varphi_{n,q}^{steer}$ is added to each subcarrier q for each antenna n, that will allow active manipulation of the geocasting target location. A mathematical expression for the steering phases is derived in Section II-D1.[1]

Subcarrier allocation is done as illustrated in Fig. 2. In the lower subcarrier range ($q < 0$), the first subcarrier is assigned to the outermost antenna, with index $n_{ref1} = 0$. The following subcarriers are systematically assigned to the neighboring antenna, heading away from the first one. Upon reaching the opposite array end, the cycle is repeated. In the upper subcarrier range ($0 \leq q$), the allocation order is reversed, starting from the opposite array edge, with index $n_{ref2} = N - 1$, following the same procedure.[2]

For equalization purposes at the receiver, the antennas n_{ref1} and n_{ref2} are referred to as the primary and complementary reference antenna, respectively. They are used to define a set of reference subcarriers $\mathcal{Q}_{ref}$. It contains in the lower subcarrier range the subcarriers assigned to the primary reference antenna, and in the upper subcarrier range those assigned to the complementary reference antenna, i.e.

$$ \mathcal{Q}_{ref} = \left\{ \mathcal{Q}_{n_{ref1}} \mid q < 0 \right\} \cup \left\{ \mathcal{Q}_{n_{ref2}} \mid 0 \leq q \right\}. \quad (2) $$

B. Propagation Channel Model

The OFDM blocks X_n are transmitted over separate antennas and hence subject to different propagation conditions. An arbitrary number of propagation paths can be present, however, a line-of-sight (LOS) component is assumed to exist in all channels. Considering that all LOS rays originate from closely placed antennas, it is assumed that they have identical complex amplitude α^{los} (i.e. path loss and overall channel phase). They are however characterized by a unique propagation delay τ_n^{los}, for each antenna n. Additionally, time variance is neglected under the quasi-static approximation. Finally, given the narrowband character of OFDM subcarriers, a frequency-flat channel is assumed in the subcarrier bandwidth of any subcarrier q. Under these conditions, the deterministic narrowband time-invariant channel transfer function $H_n[q]$, corresponding to the q-th subcarrier and n-th antenna, is given by

$$ H_n[q] = \alpha^{los}e^{-j2\pi f_q \tau_n^{los}} + \sum_{l=1}^{L_n} \alpha_l^{nlos}e^{-j2\pi f_q \tau_{n,l}^{nlos}}, \quad (3) $$

---

[1]Only a single target area is considered for the sake of clearly introducing the OFDM-SDF scheme. Multi-target OFDM-SDF is beyond the scope of this paper and constitutes the subject of future work.

[2]In practical scenarios, $Q \geq 2N$, ensuring successful subcarrier allocation.
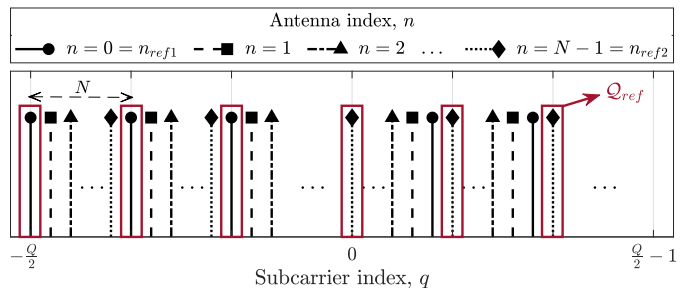

Fig. 2. Allocation of subcarriers q to antennas n. Subcarriers in the reference subcarrier set $\mathcal{Q}_{ref}$ are enclosed by a red rectangle.

where the summation includes the influence of the non line-of-sight (NLOS) channel components $l = 1, 2, \ldots, L_n$, characterized by their deterministic parameters: complex amplitude α_l^{nlos} and propagation delay $\tau_{n,l}^{nlos}$.

The transmitted symbols $X_n[q]$ are then received as $Y_n[q] = H_n[q]X_n[q] + z_n[q]$, where $z_n[q] \sim \mathcal{CN}(0, \sigma^2)$ represents complex additive white Gaussian noise, independent and identically distributed for each channel n and subcarrier q. By the exhaustive and disjoint design of the subcarrier subsets $\mathcal{Q}_n$ and the uniqueness of the transmitted symbols $X_n[q]$, the unified received OFDM block $Y[q] = \sum_{n=0}^{N-1} Y_n[q]$ carries a unique received symbol on each subcarrier $q \in \mathcal{Q}$ free from interference with other subcarriers, such that OFDM-SDF (i) does not impose array gain as in beamforming and DM, (ii) matches the spectral efficiency of conventional OFDM, and (iii) is compatible with traditional OFDM receivers.

C. Receiver: OFDM-SDF Channel Estimation & Equalization

Only the phase shift due to LOS propagation in (3) has a tractable positional dependency that can be leveraged for spatial focusing. However, this behavior is disturbed by the multipath character of the channels $H_n[q]$, prohibiting the direct exploitation of the LOS phase shift as in [25] and [27]. As a result, a twofold channel equalization is proposed for OFDM-SDF. It consists of the following complementary and consecutively applied operations:

(i) Traditional zero forcing (ZF) equalization of the channel $H_n[q]$, using its estimation $\hat{H}_n[q]$, aiming to minimize deteriorative multipath influences.

(ii) Introducing an estimation of the LOS component $\hat{H}_n^{los}[q]$ in the n-th channel on the q-th subcarrier. This is, in turn, equalized by the LOS component estimation $\hat{H}_{ref}^{los}[q_{ref}]$ of the reference channel H_{ref} evaluated at the subcarrier $q_{ref} = \arg\min_{q' \in \mathcal{Q}_{ref}, q' \leq q} |q - q'|$, i.e. the reference subcarrier that is closest to, but smaller than, the equalized subcarrier q. This step artificially re-introduces the spatially tractable LOS phase behavior, exploitable for spatial focusing as discussed in Section II-D.

The equalized symbols corresponding to the q-th subcarrier and n-th antenna are then given by

$$ \hat{Y}_n[q] = Y_n[q] \underbrace{\frac{1}{\hat{H}_n[q]}}_{(i)} \underbrace{\frac{\hat{H}_n^{los}[q]}{\hat{H}_{ref}^{los}[q_{ref}]}}_{(ii)}. \quad (4) $$

Estimation of the channel $H_n[q]$ is performed based on the transmission of an unsteered preamble symbol $P[q]$ on each subcarrier for all antennas. Based on the preamble symbols $R_n[q]$, received from the q-th subcarrier in the n-th channel, the corresponding channel transfer function estimation is given by $\hat{H}_n[q] = R_n[q]/P[q]$, as in classical OFDM.

The estimation of the LOS channel component for the q-th subcarrier in the n-th channel is defined as

$$\hat{H}_n^{los}[q] = e^{-j2\pi f_q \hat{\tau}_n^{los}}. \tag{5}$$

It emulates the tractable frequency and position dependent LOS phase shift, based on an estimation $\hat{\tau}_n^{los}$ of the LOS propagation delay in the n-th channel. Note that an estimation of the LOS complex amplitude α^{los} is not included or required in (5), as the ratio (ii) in (4) is independent of its value. Its estimation and equalization are embedded in the ZF stage (i), however.

Under the assumption of transmitter-receiver synchronization to a common time reference, a coarse estimation $\tilde{\tau}_n^{los}$ of the n-th channel's LOS propagation delay can be obtained. Assuming an antenna spacing in the same order of magnitude as the carrier wavelength, then for gigahertz carrier frequencies and above, sub-nanosecond propagation delay differences exist between antennas in the array. As a result, for bandwidths in the megahertz order of magnitude, the time resolution is insufficient to yield an accurate representation of differences in LOS delay between channels. However, a value averaged over all channel indices yields an estimate of the propagation delay from the array's center, i.e.

$$\bar{\tau}^{los} = \frac{1}{N} \sum_{n=0}^{N-1} \tilde{\tau}_n^{los}. \tag{6}$$

A more accurate estimation of the difference in LOS delay between channels is obtained from the channel impulse response (CIR) $\hat{h}_n[m]$ (m being the discrete time or tap index), calculated through inverse discrete Fourier transform (IDFT) of the corresponding channel transfer function estimation $\hat{H}_n[q]$. More specifically, the LOS delay difference between neighboring antennas in the array is inferred from the CIR phase difference between them, in the tap $\bar{m}^{los}$ that corresponds to the identified average LOS delay $\bar{\tau}^{los}$. Averaging this value over all pairs of neighboring antennas yields an average $\overline{\Delta\tau}^{los}$, representing the constant LOS delay difference expected between neighboring channels, i.e.

$$\overline{\Delta\tau}^{los} = \frac{1}{(N-1)} \sum_{n=0}^{N-2} \frac{\angle \hat{h}_{n+1}[\bar{m}^{los}] - \angle \hat{h}_n[\bar{m}^{los}]}{-2\pi f_c}. \tag{7}$$

Therefore, the estimation $\hat{\tau}_n^{los}$ of the n-th channel's LOS propagation delay in (5) can be defined as

$$\hat{\tau}_n^{los} = \bar{\tau}^{los} + (n - \tfrac{N-1}{2})\overline{\Delta\tau}^{los}. \tag{8}$$

Using the above estimation (5) of the LOS channel component and assuming perfect equalization of the multipath channel $H_n[q]$ in (4),[3] the following expression is found for

[3] This allows to isolate and independently analyze the behavior introduced by the second equalization stage in (4). Section II-E addresses the implications of imperfect multipath channel equalization.

the equalized symbols received from the q-th subcarrier in the n-th channel

$$\hat{Y}_n[q] = \begin{cases} S[q]e^{j\varphi_{n,q}^{steer}} e^{-j2\pi f_q \Delta\hat{\tau}_n^{los}} e^{-j2\pi\Delta q B_c \hat{\tau}_{ref}^{los}} \\ \qquad\qquad\qquad\qquad q \in \mathcal{Q}_n \quad + z_n'[q]. \\ 0 \qquad\qquad\qquad q \in \mathcal{Q} \setminus \mathcal{Q}_n \end{cases} \tag{9}$$

In (9), z_n' is the noise vector after undergoing the equalization (4), and $\Delta\hat{\tau}_n^{los} = \hat{\tau}_n^{los} - \hat{\tau}_{ref}^{los}$ and $\Delta q B_c = (q - q_{ref})B_c$, $\Delta q = 0, 1, \ldots, N - 1$ express, respectively, the difference in estimated LOS delay and in frequency, between the channel corresponding to the n-th antenna and q-th subcarrier, and the reference channel corresponding to the reference subcarrier q_{ref}.

Note that OFDM-SDF processing and thus computational complexity correspond to that of N single-input single-output (SISO) OFDM links. The supplementary IDFT operation for the CIR estimation used in (7) does not raise the overall order of magnitude, as it is embedded in OFDM processing as well.

D. Spatial Confinement of Correct Data Retrieval

The equalized symbols (9) are distorted by a residual phase shift and perfect retrieval of the transmitted information is hence only possible on the condition that this phase shift is equal to an integer multiple of 2π, i.e.

$$\varphi_{n,q}^{steer} - 2\pi f_q \Delta\hat{\tau}_n^{los} - 2\pi\Delta q B_c \hat{\tau}_{ref}^{los} = k2\pi, \quad k \in \mathbb{Z}. \tag{10}$$

The expected spatial behavior of this phase condition becomes clear by observing the theoretical counterparts of the estimations $\Delta\hat{\tau}_n^{los}$ and $\hat{\tau}_{ref}^{los}$. Under the paraxial approximation ($b \ll d$), they are respectively given by

$$\Delta\tau_n^{los} = -\Delta n \frac{b}{c} \sin\theta, \tag{11a}$$

$$\tau_{ref}^{los} = \frac{d}{c} - (n_{ref} - \tfrac{N-1}{2})\frac{b}{c}\sin\theta, \tag{11b}$$

where c is the speed of light and $\Delta n = n - n_{ref} = 0, \pm 1, \ldots, \pm(N-1)$ represents the index difference between the n-th and reference antenna $n_{ref} = n_{ref1}, n_{ref2}$.

1) Steering Phases: Given the right choice of steering phase in the transmitted symbols (1), the solution of (10) can be actively manipulated to coincide with an arbitrary target position $(d^{steer}, \theta^{steer})$. From (10), one finds

$$\varphi_{n,q}^{steer} = 2\pi\big[k + f_q\Delta\hat{\tau}_n^{los} + \Delta q B_c \hat{\tau}_{ref}^{los}\big]. \tag{12}$$

The integer k can be omitted as it modifies the required steering phase by multiples of 2π only. The final expression of the steering phases is then found after substituting $\Delta\hat{\tau}_n^{los}$ and $\hat{\tau}_{ref}^{los}$ by their theoretical counterparts (11a) and (11b), evaluated at the target position $(d^{steer}, \theta^{steer})$. The steering phase to be added to the symbols on the q-th subcarrier of the n-th antenna then becomes

$$\varphi_{n,q}^{steer} = 2\pi\Bigg[\frac{\Delta q B_c}{c}d^{steer} - \Big(\Delta n f_q + \Delta q B_c(n_{ref} - \tfrac{N-1}{2})\Big)\frac{b}{c}\sin\theta^{steer}\Bigg]. \tag{13}$$

Note that OFDM-SDF precoding uses only the target location coordinates $(d^{steer}, \theta^{steer})$ and no individual user channel state information (CSI), complying to geocasting's location-based rather than user-based nature and respecting its privacy prospects. In practice, the target location is selected by the transmitter based on the application, hence its coordinates are a priori quasi-static and perfectly known upon transmission. As a result, OFDM-SDF precoding is invariant to the amount of users, their relative position and movement, and requires no user localization, as opposed to user-based focusing.

2) Data Focusing: After substitution of $\Delta\hat{\tau}_n^{los}$ and $\hat{\tau}_{ref}^{los}$ by their theoretical counterparts (11a) and (11b), the phase condition (10) yields an expression of the radial distance d, as a function of the azimuth angle θ, at which the symbol stream on the q-th subcarrier of the n-th channel is correctly retrieved

$$
\begin{aligned}
d(\theta) = \frac{c}{\Delta q B_c}&\left(k + \frac{\varphi_{n,q}^{steer}}{2\pi}\right) \\
&+ \left(\frac{\Delta n}{\Delta q}\frac{f_q}{B_c} + (n_{ref} - \tfrac{N-1}{2})\right)b\sin\theta, \quad \Delta q \neq 0.
\end{aligned}
\tag{14}
$$

Interpretation of this expression is simplified significantly by noting that: (i) assuming narrowband approximation $B_c \ll f_c$ yields $f_c/B_c \approx f_q/B_c \gg (n_{ref} - \tfrac{N-1}{2})$; (ii) $\Delta q = |\Delta n|$ for the subcarrier allocation in Fig. 2, such that $\frac{\Delta n}{\Delta q} = \text{sgn}(\Delta n)$, making the patterns (14) unique for the data from each antenna n, differing only in their period $\frac{c}{\Delta q B_c}$ along the radial axis; and (iii) simultaneous undistorted recovery of all datastreams is achieved only where the curves (14) coincide for all antennas, which can occur only at the rate given by the largest radial periodicity, i.e. $\frac{c}{B_c}$ for $\Delta q = |\Delta n| = 1$. As a result, perfect retrieval of transmitted information from all antennas is achieved at the positions satisfying

$$
d(\theta) \approx \frac{c}{B_c}\left(k + \frac{\varphi_{n^*,q^*}^{steer}}{2\pi}\right) + \text{sgn}(\Delta n)\frac{f_c}{B_c}b\sin\theta,
\tag{15}
$$

where $\text{sgn}(\cdot)$ is the sign function and the superscript * on the antenna and subcarrier index indicates that the steering phase corresponding to the antenna that complies with $|\Delta n| = \Delta q = 1$ should be used, in correspondence with the assumptions above.

Through the double reference channel use, two of the above patterns (15) are created, applying to the data transmitted in the respective subcarrier ranges of the two reference channels. As a result of the symmetrical reference antenna choice, they are symmetrical as well, differing only in the value of $\text{sgn}(\Delta n)$. Perfect equalization on all subcarriers $q \in \mathcal{Q}$, and hence correct recovery of the full datastream, is only realized at the intersection of both patterns, i.e. when

$$
\begin{aligned}
\frac{c}{B_c}&\left(k_1 + \frac{\varphi_{n_1^*,q_1^*}^{steer}}{2\pi}\right) + \frac{f_c}{B_c}b\sin\theta \\
&= \frac{c}{B_c}\left(k_2 + \frac{\varphi_{n_2^*,q_2^*}^{steer}}{2\pi}\right) - \frac{f_c}{B_c}b\sin\theta,
\end{aligned}
\tag{16}
$$

where subscripts 1 and 2 indicate the use of parameters corresponding to, respectively, the primary and complementary reference channel.

Solving (16) for θ and substituting its solution(s) in (15) yields an expression for the polar coordinates (d, θ) at which perfect data recovery is achieved.[4] One finds

$$
d \approx \frac{1}{2}\frac{c}{B_c}\left(k' + \frac{\varphi_{n_1^*,q_1^*}^{steer} + \varphi_{n_2^*,q_2^*}^{steer}}{2\pi}\right),
\tag{17a}
$$

$$
\theta = \arcsin\left(\frac{1}{2}\frac{\lambda_c}{b}\left(k'' + \frac{\varphi_{n_2^*,q_2^*}^{steer} - \varphi_{n_1^*,q_1^*}^{steer}}{2\pi}\right)\right),
\tag{17b}
$$

where $k' = k_1 + k_2 \in \mathbb{Z}$ and $k'' = k_2 - k_1 \in \mathbb{Z}$, and $\lambda_c = c/f_c$ is the carrier wavelength. Using (13), exploiting again that $f_c/B_c \approx f_q/B_c \gg (n_{ref} - \tfrac{N-1}{2})$, and noting that the superscript * was introduced to imply $|\Delta n| = \Delta q = 1$, one finds that $(\varphi_{n_1^*,q_1^*}^{steer} + \varphi_{n_2^*,q_2^*}^{steer})/2\pi = 2\frac{B_c}{c}d^{steer}$ and $(\varphi_{n_2^*,q_2^*}^{steer} - \varphi_{n_1^*,q_1^*}^{steer})/2\pi = 2\frac{b}{\lambda_c}\sin\theta^{steer}$. As a result, (17a) and (17b) become

$$
d \approx d^{steer} + \frac{1}{2}\frac{c}{B_c}k',
\tag{18a}
$$

$$
\theta = \arcsin\left(\sin\theta^{steer} + \frac{1}{2}\frac{\lambda_c}{b}k''\right).
\tag{18b}
$$

While a solution of the phase condition for perfect data retrieval (10) is ensured at the target position $(d^{steer}, \theta^{steer})$, its uniqueness is not guaranteed in general due to the presence of the integers k' and k''. As a consequence, potential spurious regions in both the radial and azimuthal domain where data is undesirably retrievable should be mitigated.

3) Spatial data retrieval uniqueness: In the azimuthal domain, uniqueness of perfect data retrieval is ensured when the only solution of (18b) is given for $k'' = 0$, i.e. when

$$
\left|\sin\theta^{steer} + \frac{1}{2}\frac{\lambda_c}{b}k''\right| > 1, \quad \forall k'' \in \mathbb{Z}_0.
\tag{19}
$$

Noting that the most strict condition is obtained for $|k''| = 1$ and that the antenna spacing $b > 0$, one finds an upper bound for the antenna spacing that ensures azimuthal uniqueness:

$$
b < \frac{1}{2}\frac{1}{1 + |\sin\theta^{steer}|}\lambda_c.
\tag{20}
$$

Due to the periodicity of (18a) and the infinite character of the radial axis, uniqueness in this dimension cannot be guaranteed in theory. However, if no solution of (18a) exists in the ranges $[0, d^{steer}[$ and $]d^{steer}, d^{lim}]$, where d^{lim} is the distance at which signal attenuation is sufficient or a physical barrier exists to prevent data recovery, then practical uniqueness is ensured. This translates into the following condition:

$$
\begin{cases}
d^{steer} + \frac{1}{2}\frac{c}{B_c}k' < 0 & \forall k' \in \mathbb{Z}_0^- \\
d^{lim} < d^{steer} + \frac{1}{2}\frac{c}{B_c}k' & \forall k' \in \mathbb{Z}_0^+.
\end{cases}
\tag{21}
$$

Given that $k'' = k_2 - k_1 = 0$ is imposed by the conditions for azimuthal uniqueness, it is implied that $k_1 = k_2$, such that $k' = k_1 + k_2$ is an even integer. The most strict bounds in (21)

---

[4] Assuming the use of either the primary or complementary reference channel's parameters upon substitution in (15) yields identical results.

are thus found for $|k'| = 2$. As a result, one finds that radial uniqueness is ensured when the subcarrier bandwidth satisfies

$$B_c < \min\left\{\frac{c}{d^{steer}}, \frac{c}{d^{lim} - d^{steer}}\right\}. \tag{22}$$

Note that, in practice, every position that yields a solution of (18a) and (18b) is surrounded by a non negligible area where symbol distortion remains sufficiently small to allow correct data retrieval. Thus, the practical upper bounds on b and B_c should be chosen slightly below their theoretical upper bounds, of which an approximate value is hence sufficient. As a result, the approximations made at the start of this section are justified.

4) Geocast delivery zone: While the above discussion proves that OFDM-SDF-induced symbol distortion is zero in the target position $(d^{steer}, \theta^{steer})$ only, communication is possible in a nonzero 2-dimensional interval around it, where no symbol errors are induced by the residual phase shift in (9). Assuming a noiseless free space scenario, this is guaranteed for the positions (d, θ) where the residual phase shift is bounded by Φ_{th}, defined as the phase shift at which the first symbol error occurs for a given constellation. One finds

$$-\Phi_{th} < \pm 2\pi(N-1)\frac{b}{\lambda_c}\left[\sin\theta - \sin\theta^{steer}\right] \\ - 2\pi(N-1)\frac{B_c}{c}\left[d - d^{steer}\right] < \Phi_{th}, \tag{23}$$

where the residual phase shift expression is obtained from the left-hand side of (10) after (i) substituting $\Delta\hat{\tau}_n^{los}$ and $\hat{\tau}_{ref}^{los}$ by their theoretical counterparts (11a) and (11b); (ii) inserting the steering phase expression (13); (iii) assuming narrowband approximation $B_c \ll f_c \approx f_q$; and (iv) noting that, under the established subcarrier allocation and reference antenna conventions, it is maximal for $|\Delta n| = \Delta q = N - 1$.

Solving the inequality (23) for d and θ yields the lower and upper bounds of, respectively, the radial and angular intervals in which no symbol errors occur, i.e. the geocast delivery zone. In the process, the variable sign in (23) should be chosen such that the most strict bounds are found. Subtracting the lower bounds from the corresponding upper bound yields the radial $\Theta_d(\theta)$ and angular $\Theta_\theta(d)$ width of the geocast delivery zone (i.e. geocast-width) as a function of the receiver azimuth

and radial position. They are shown in (24a) and (24b) at the bottom of this page. While not constant, they are maximal at, respectively, θ^{steer} and d^{steer}, where they are equal to

$$\Theta_d = 2\frac{\Phi_{th}}{2\pi}\frac{c}{(N-1)B_c} \tag{25a}$$

$$\Theta_\theta = \arcsin\left(\sin\theta^{steer} + \frac{\Phi_{th}}{2\pi}\frac{\lambda_c}{(N-1)b}\right) \\ - \arcsin\left(\sin\theta^{steer} - \frac{\Phi_{th}}{2\pi}\frac{\lambda_c}{(N-1)b}\right). \tag{25b}$$

The value of the residual phase shift threshold Φ_{th} depends on the employed constellation. For M-PSK and square M-QAM, it is respectively given by

$$\Phi_{th}^{PSK} = \frac{\pi}{M} \tag{26a}$$

$$\Phi_{th}^{QAM} = \frac{\pi}{4} - \arcsin\left(\frac{\sqrt{2}(\sqrt{M} - 2)}{2(\sqrt{M} - 1)}\right). \tag{26b}$$

It can easily be determined for other constellations as the smallest phase difference between any symbol and the closest decision boundary with its neighbors in the constellation.

E. Channel Coding and Symbol Mapping

As proven in Section II-D, around the geocasting target location, the residual OFDM-SDF phase shift in (9) is negligible. Hence, only the first stage in the equalization (4) remains, such that it acts as traditional OFDM ZF. While perfect multipath channel equalization was assumed in Section II-C, in practical scenarios it is deteriorated by noise and other imperfections. Thus, to increase robustness in the geocast delivery zone and combat bit-level errors introduced by imperfect multipath equalization that would raise the BER of OFDM-SDF inside its geocast delivery zone, channel coding, e.g. low-density parity-check (LDPC) [28], can be used, as in classical OFDM.
The employed LDPC parity-check matrix is configured according to the DVB-S2 standard, with a code rate of $1/2$. Iterations are performed until the parity-check is satisfied or until a maximum iteration count of 15 is reached.

As it operates on the bit-level, LDPC coding undermines the underlying symbol-level SDF operation due to its inability to distinguish between channel-caused and SDF-caused bit

$$\Theta_d(\theta) = \begin{cases} 2\frac{\Phi_{th}}{2\pi}\frac{c}{(N-1)B_c} + 2\frac{bf_c}{B_c}[\sin\theta - \sin\theta^{steer}] & \theta \leq \theta^{steer} \\ 2\frac{\Phi_{th}}{2\pi}\frac{c}{(N-1)B_c} - 2\frac{bf_c}{B_c}[\sin\theta - \sin\theta^{steer}] & \theta^{steer} \leq \theta \end{cases} \tag{24a}$$

$$\Theta_\theta(d) = \begin{cases} \arcsin\left(\sin\theta^{steer} + \frac{\Phi_{th}}{2\pi}\frac{\lambda_c}{(N-1)b} + \frac{B_c}{bf_c}[d - d^{steer}]\right) - \arcsin\left(\sin\theta^{steer} - \frac{\Phi_{th}}{2\pi}\frac{\lambda_c}{(N-1)b} - \frac{B_c}{bf_c}[d - d^{steer}]\right) \\ \hfill d \leq d^{steer} \\ \arcsin\left(\sin\theta^{steer} + \frac{\Phi_{th}}{2\pi}\frac{\lambda_c}{(N-1)b} - \frac{B_c}{bf_c}[d - d^{steer}]\right) - \arcsin\left(\sin\theta^{steer} - \frac{\Phi_{th}}{2\pi}\frac{\lambda_c}{(N-1)b} + \frac{B_c}{bf_c}[d - d^{steer}]\right) \\ \hfill d^{steer} \leq d \end{cases} \tag{24b}$$
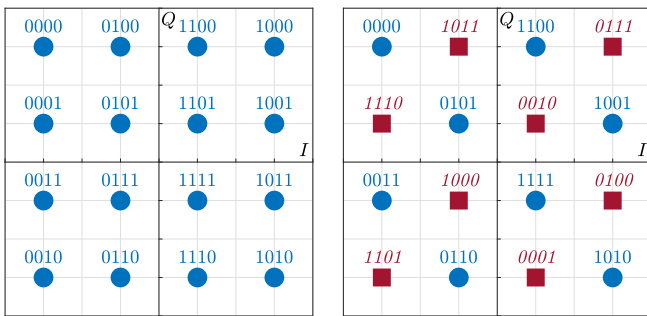
Fig. 3. 16-QAM constellation: Gray code symbol mapping (left); Semi-inverted Gray code symbol mapping (right). Red squares and italics indicate symbols with bit-wise complemented binary sequences.

errors. While correction of the former is desired and essential, correction of the latter counteracts the principal goal of SDF. Indeed, when a conventional Gray code ordered symbol constellation is used, first-tier symbol errors caused by the residual SDF phase shift generate single bit errors that are easily corrected by the LDPC decoder. Hence leading to a widening of the geocast delivery zone and an undesired decrease in precision of the scheme.

This is mitigated by introducing a semi-inverted Gray code ordered symbol constellation. It consists in replacing the binary sequence for every other symbol in any arbitrary Gray code ordered constellation by its bit-wise complement. Thus, a Hamming distance of $k-1$ is ensured between neighboring symbols when k bits per symbol are used. Additionally, single Hamming distance symbols are ensured to be each other's third nearest neighbor at least. In this way, near-neighbor symbol errors are maximally penalized, such that a high BER enforced by SDF is retained even after LDPC decoding. This approach is illustrated in Fig. 3 for a 16-QAM constellation.

III. PRACTICAL GEOCAST DELIVERY ZONE IDENTIFICATION & EVALUATION

In practical scenarios, a geocast delivery zone deviates from its ideal shape due to noise, multipath propagation, LDPC coding, resolution limitations, etc. that are not taken into account in the theoretical derivation of Section II-D4. Hence, practical identification and evaluation of a geocast zone should not rely on the symbol distortion, but is instead accomplished by describing the spatial BER distribution.

A. Identification

The geographical region in which a receiver can correctly recover transmitted information is described by the set $\mathcal{L}$ of positions in which the BER is below a threshold BER_{max}, i.e.

$$\mathcal{L} = \left\{ (d,\theta) \big| BER(d,\theta) < BER_{max} \right\}. \quad (27)$$

Due to the envisioned focusing properties of SDF, or any geocasting scheme, the positions in this set are expected to be spatially clustered together. They can thus be characterized using spatial clustering algorithms.

In particular, density-based spatial clustering of applications with noise (DBSCAN) [29] is used for its ability of detecting

outliers and arbitrarily shaped clusters. Based on the input parameters $MinPts$ and ε, DBSCAN identifies clusters consisting of core and edge points, and complementary noise points or outliers. It is shown in [29] that $MinPts = 4$ is an optimal value for 2-dimensional data, after which the corresponding value for ε is found as the first threshold point in the sorted graph of k-th nearest neighbor distances for each point, i.e. the sorted k-distance graph, with $k = MinPts$. Applied to the positions in the set $\mathcal{L}$, the DBSCAN algorithm, yields the subsets $\mathcal{L}_{core}$, $\mathcal{L}_{edge}$, and $\mathcal{L}_{out}$ of respectively the core and edge low BER cluster positions, and the low BER outliers.

In general, the cluster of low BER positions is not continuous and positions with high BER may be scattered between them. Let $\mathcal{H}$ be the complementary set of $\mathcal{L}$, i.e. the set of all positions at which the BER is above or equal to the threshold BER_{max}

$$\mathcal{H} = \left\{ (d,\theta) \big| BER(d,\theta) \geq BER_{max} \right\}. \quad (28)$$

Then, the set $\mathcal{H}_{out}$ of high BER outliers within the low BER cluster can be identified by applying the DBSCAN algorithm on the set $\mathcal{H} \cup \mathcal{L}_{out}$ of all positions not belonging to the low BER cluster.

Finally, the geocast delivery zone is defined as the continuous geographical region spanned by the positions in the set

$$\mathcal{G} = \mathcal{L}_{core} \cup \mathcal{L}_{edge} \cup \mathcal{H}_{out}. \quad (29)$$

Potential deterioration is characterized by the high $\mathcal{H}_{out}$ and low $\mathcal{L}_{out}$ BER outliers that respectively prohibit data retrieval inside the delivery zone and allow data retrieval outside of it. A practical example and visualization of the results obtained by this procedure is given in Fig. 9 of Section IV.

It should be noted that DBSCAN is limited by the inability to specify the number of expected clusters. Thus, possibly, multiple low BER clusters $\{\mathcal{L}_{core}^1 \cup \mathcal{L}_{edge}^1\}, \{\mathcal{L}_{core}^2 \cup \mathcal{L}_{edge}^2\}, \ldots$ may be detected, in which case only the largest cluster is retained and all others are added to the outlier set $\mathcal{L}_{out}$. A similar approach is undertaken for the identification of high BER outliers. This corresponds to a worst-case representation of the performance metrics defined in the next section.

B. Evaluation

1) Geocast-width – Precision and Spatial Variability: The practical radial and azimuthal geocast-widths, $\widehat{\Theta}_d$ and $\widehat{\Theta}_\theta$, can be defined respectively as the radial and azimuthal range covered by the geocast delivery zone positions $(d,\theta) \in \mathcal{G}$, i.e.

$$\widehat{\Theta}_d = \max \left\{ d \big| (d,\theta) \in \mathcal{G} \right\} - \min \left\{ d \big| (d,\theta) \in \mathcal{G} \right\}, \quad (30a)$$

$$\widehat{\Theta}_\theta = \max \left\{ \theta \big| (d,\theta) \in \mathcal{G} \right\} - \min \left\{ \theta \big| (d,\theta) \in \mathcal{G} \right\}. \quad (30b)$$

They are the main metrics to assess a delivery zone's dispersion around its centroid, i.e. the geocasting precision. Note that by replacing the set $\mathcal{G}$ by the set $\mathcal{G} \cup \mathcal{L}_{out}$ in the above definitions, the outlier-inclusive radial and

azimuthal geocast-widths, $\widehat{\Theta}_d^{out}$ and $\widehat{\Theta}_\theta^{out}$, can be obtained. They describe the system's spatial variability as a result of deterioration due to low BER outliers.

Both above metrics can be divided by their theoretical counterparts (25a) and (25b) to obtain a normalized representation.

2) Delivery Zone Connectivity: Deterioration due to high BER outliers inside the geocast zone is quantified by its connectivity C. It is defined as the ratio of the number of low BER positions and the total number of positions inside the geocast delivery zone, i.e.

$$C = \frac{\text{card}(\mathcal{L}_{core} \cup \mathcal{L}_{edge})}{\text{card}(\mathcal{G})}, \quad (31)$$

where $\text{card}(\cdot)$ is the cardinality operator.

IV. SIMULATIONS AND PERFORMANCE EVALUATION

Simulations are performed in free space and multipath scenarios. For straightforward evaluation of the scheme as a function of the Rice factor, the deterministic channel (3) is modeled by a normalized Rice channel. For the n-th antenna and q-th subcarrier, it is defined as

$$\tilde{H}_n^{Rice}[q] = \sqrt{\frac{K}{K+1}} \tilde{H}_n^{los}[q] + \sqrt{\frac{1}{K+1}} \tilde{H}_n^{Ray}[q]. \quad (32)$$

$\tilde{H}_n^{los}[q]$ is the unit-power LOS transfer function of the corresponding antenna and subcarrier. It is deterministic and can be calculated exactly for each simulated receiver position. $\tilde{H}_n^{Ray}[q]$ is a stochastic component modeling the aggregation of all NLOS channel components. Its amplitude follows a normalized Rayleigh distribution and its phase is uniformly distributed between 0 and 2π. Independent realizations of this channel component are performed for each antenna, subcarrier, and simulated receiver position. The relative power of the LOS and NLOS component is weighted by the Rice factor K. By taking $\lim_{K \to \infty} \tilde{H}_n^{Rice}$, the free space channel is obtained.

The following system parameters are used. The steering range and angle are, respectively, $d^{steer} = 100$ m and $\theta^{steer} = 20°$. The antenna spacing and subcarrier bandwidth are set to $b = 0.325\lambda_c$ and $B_c = 781.25$ kHz (with $B = 100$ MHz and $Q = 128$), in compliance with (20) and (22). The number of antennas N is varied and the carrier frequency is $f_c = 3.6$ GHz. The transmitted bitstream has length 10^5 and is mapped onto a 16 QAM constellation, following the semi-inverted Gray code in Fig. 3. A fixed SNR of 25 dB is imposed at all receiver positions. The simulation grid has a radial and angular resolution of $\Delta d_{sim} = 0.90$ m and $\Delta\theta_{sim} = 0.44°$ respectively, corresponding to 2.5% of the theoretical geocast-widths $\Theta_d = 36.0$ m and $\Theta_\theta = 17.7°$, as given by (25a) and (25b) respectively.

Fig. 4 shows the 2-dimensional BER distribution that is obtained in free space when applying the proposed channel estimation and equalization from Section II-C to the signals received from an OFDM-SDF array with $N = 2$ antennas, aligned with the y-axis and centered around the origin. It shows a unique and bounded region of low BER, centered around the target position, as desired. Some areas exist with a BER slightly below the average value outside the geocast delivery zone. However, this effect is easily suppressed by increasing the number of antennas. This implies a decrease in the number of reference subcarriers, thus decreasing the amount of symbols unaffected by OFDM-SDF distortion and effectively increasing the BER outside the delivery zone.

Figs. 5 and 6 analyze, respectively, the radial and angular precision of the proposed OFDM-SDF scheme in free space, as a function of the number of antennas N. These results are compared to the theoretical SDF geocast-widths (25a) and (25b), random-subcarrier-selection-based OFDM directional modulation (RSCS-OFDM-DM) [18], and, where applicable, preliminary SDF implementations [25] and [27].

First, it is shown that the proposed semi-inverted Gray code symbol mapping (s-i Gr.) is indeed beneficial to counteract delivery zone widening that results from combining OFDM-SDF with LDPC channel coding and traditional Gray code symbol mapping (Gr.). While the proposed scheme remains fully functional in the latter scenario, its geocast-width differs from the theoretical values by a factor of 2 approximately, while the former succeeds in approximating
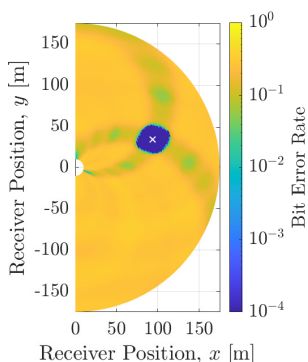

Fig. 4. Free space OFDM-SDF BER distribution for $N = 2$ antennas. White $\times$ marks target position ($d^{steer} = 100$ m, $\theta^{steer} = 20°$).
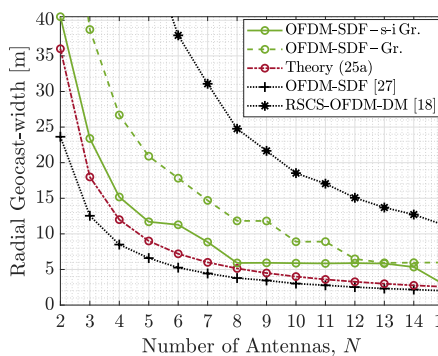

Fig. 5. Free space radial geocast-width around target position ($d^{steer} = 100$ m, $\theta^{steer} = 20°$), for varying number of antennas N.
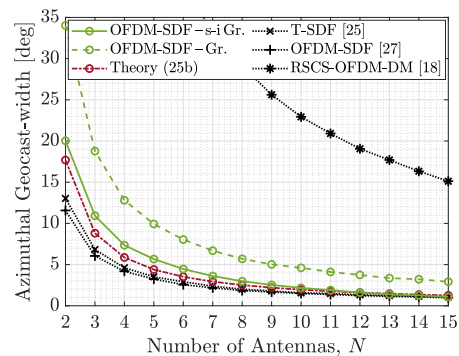

Fig. 6. Free space azimuthal geocast-width around target position ($d^{steer} = 100$ m, $\theta^{steer} = 20°$), for varying number of antennas N.
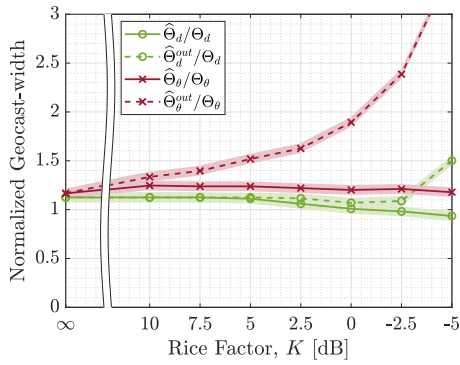
Fig. 7. Geocast-width and outlier-inclusive geocast-width (normalized) for decreasing Rice factor K. Shading shows uncertainty ($\pm 2\Delta d_{sim}$, $\pm 2\Delta\theta_{sim}$) due to discretized simulation grid.
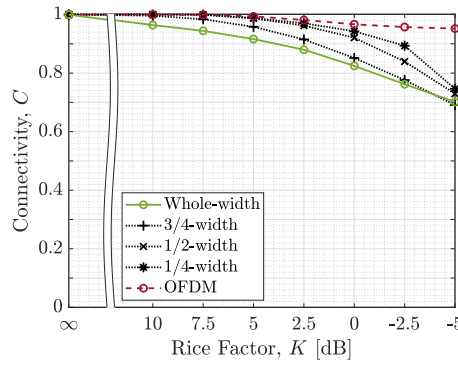
Fig. 8. OFDM-SDF geocast delivery zone connectivity for decreasing Rice factor K, compared to classical SISO OFDM connectivity.
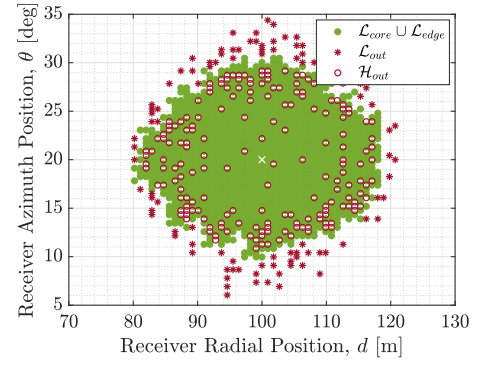
Fig. 9. Clustering results for OFDM-SDF geocast delivery zone identification at Rice factor $K = 2.5$ dB and target position ($d^{steer} = 100$ m, $\theta^{steer} = 20°$), marked by white $\times$.

the theoretical values more closely, as anticipated in Section II-E. Additionally, in contrast to [25] and [27], that suffer from noise-caused narrowing and undershoot the theoretical geocast-widths, the proposed scheme remains above and in better approximation of these reference values.

The discontinuous decrease of the radial geocast-width in Fig. 5 is a consequence of the limited resolution $\Delta\tau_{est}$ for the estimation of the absolute LOS delay $\tilde{\tau}_n^{los}$ in (6), which determines the radial dependency of the residual phase shift on the received OFDM-SDF symbols (9). Hence, the radial geocast-width can only vary by multiples of the corresponding radial resolution $\Delta d_{est} = c\Delta\tau_{est}$. For the employed bandwidth, this corresponds to $\Delta d_{est} = 3$ m.

Most importantly, Figs. 5 and 6 prove OFDM-SDF's superior precision over DM literature: a 2-antenna OFDM-SDF array matches the radial and angular precision of, respectively, a 6 and 12-antenna RSCS-OFDM-DM array. The latter results are obtained by enforcing complex Gaussian interference to a SISO link according to the closed-form signal-to-interference-plus-noise ratio spatial distribution (37) in [18] and observing the resulting BER – LDPC and semi-inverted Gray code symbol mapping are applied for a fair comparison. The physical array size (spacing and number of antennas) is set equal to OFDM-SDF and the bandwidth is set such that the inter-antenna frequency difference expected value matches OFDM-SDF's maximal frequency offset, for a fair angular and radial precision comparison, respectively. $1/4$ of power is allocated to the useful signal, yielding minimal geocast-width when LDPC is used. Besides improved precision, OFDM-SDF avoids spectral efficiency sacrifices as in [18], where a majority of subcarriers remains idle. Moreover, OFDM-SDF can operate with a minimal number of 2 antennas, whereas [18] requires medium-scale to large-scale arrays to successfully exploit the random subcarrier selection nature for signal scrambling in undesired directions.

Quantification of OFDM-SDF's performance in multipath channels for decreasing Rice factor is done in Figs. 7 and 8 for $N = 2$ antennas, showing respectively the normalized geocast-width and delivery zone connectivity, as defined in Section

III-B. Following the approach in Section III-A, the BER threshold for delivery zone identification is $BER_{max} = 10^{-3}$ and the first threshold point in the sorted k-distance graphs with $k = MinPts = 4$ yields values of 1.1 and 1.5 for the DBSCAN parameter ε, for the clustering of $\mathcal{L}$ and $\mathcal{H} \cup \mathcal{L}_{out}$ respectively. Note that the data features d and θ have different physical dimensions, such that their values should be normalized by the respective simulation grid resolution before clustering, i.e. $d' = d/\Delta d_{sim}$ and $\theta' = \theta/\Delta\theta_{sim}$, to yield a common (normalized) ε value. The resulting clustering and identified geocast delivery zone are illustrated in Fig. 9 for a Rice factor of $K = 2.5$ dB. At the investigated Rice factors, the SDF techniques in [25] and [27] are unable to create any low BER region, making a formal comparison impossible, however emphasizing the improved robustness provided by the proposed scheme. Similarly, [18] does not consider a multipath scenario.

From Fig. 7 it can be seen that the normalized geocast-widths $\widehat{\Theta}_d/\Theta_d$ and $\widehat{\Theta}_\theta/\Theta_\theta$ remain close to one, regardless of the Rice factor. Indicating a system precision invariant to the Rice factor, and proving good approximation of the theoretical noiseless free space geocast-width, even in noisy multipath scenarios. Additionally, a near-zero spatial variability in the radial domain can be observed as the radial outlier-inclusive geocast-width $\widehat{\Theta}_d^{out}$ differs only from the radial geocast-width $\widehat{\Theta}_d$ at very low Rice factors. A non-zero spatial variability in the angular domain does create an angular transition region of low BER outliers outside the delivery zone, whose size depends on the Rice factor. This is confirmed by Fig. 9, where low BER outliers $\mathcal{L}_{out}$ spread out more in the azimuthal dimension than the radial dimension.

While, in Fig. 8, the OFDM-SDF whole-width geocast delivery zone connectivity decreases at lower Rice factors, it should be noted that, as illustrated by Fig. 9, most high BER outliers $\mathcal{H}_{out}$ are concentrated in proximity of the delivery zone's edge, where the residual phase shift in (9) is elevated and hence more easily distorted to above-threshold values. To this end, one can study the $3/4$, $1/2$, and $1/4$-width connectivity in Fig. 8, obtained as the connectivity in the elliptical regions around the target location with axis length of, respectively,

3/4, 1/2, or 1/4 times the OFDM-SDF geocast-widths. The latter two in particular show that, as anticipated, the OFDM-SDF connectivity in the region closest to the target position approaches the performance of traditional SISO OFDM, for Rice factors up to $K = 0$ dB. This condition is satisfied in 5G small cell channels, both at millimeter-wave [30] and microwave [31] frequencies, showing OFDM-SDF's practical prospects.

V. CONCLUSION AND PERSPECTIVES

In this paper, OFDM-based spatial data focusing (OFDM-SDF) is proposed as a novel means of performing wireless physical-layer geocasting, i.e. spatially confined broadcasting. It improves on beamforming and directional modulation (DM) shortcomings by offering higher precision with a reduced number of antennas and uncoupled range-angle-dependent focusing. Additionally, it introduces multipath robustness into the spatial data focusing (SDF) framework, previously limited to free space use cases.

A formal system model describes improved multipath-resilient OFDM-SDF channel equalization and the analytical derivation of steering phases, closed-form geocast delivery zone expressions and conditions for sidelobe mitigation, to allow straightforward system design as a function of, respectively, target position, precision requirements, and ensured delivery zone uniqueness. An approach for practical identification and evaluation of a geocast delivery zone, using density-based clustering of the spatial BER distribution, is proposed and leads to the definition of precision, spatial variability, and connectivity metrics.

A simulation-based analysis of the proposed scheme in Rice channels has shown that: (i) OFDM-SDF outperforms existing literature, by matching the radial and angular precision of, respectively, a 6 and 12-antenna DM array in [18] with only 2 antennas; (ii) Free space precision is maintained regardless of the Rice factor; (iii) Spatial variability through low BER outliers is non-negligible in the angular domain only; (iv) OFDM-SDF connectivity around the geocast target position approaches classical SISO OFDM connectivity up to Rice factors of 0 dB, adequate for operation in 5G small cells.

REFERENCES

[1] M. Di Felice, L. Bedogni, and L. Bononi, "Group communication on highways: An evaluation study of geocast protocols and applications," *Ad Hoc Networks*, vol. 11, no. 3, pp. 818–832, May 2013.

[2] Q. Yu and G. Heijenk, "Abiding geocast for warning message dissemination in vehicular ad hoc networks," in *ICC Workshops - 2008 IEEE International Conference on Communications Workshops*, Beijing, China, May 2008, pp. 400–404.

[3] J. C. Navas and T. Imielinski, "Geocast – geographic addressing and routing," in *Proceedings of the 3rd annual ACM/IEEE international conference on Mobile computing and networking*, Budapest, Hungary, Sep. 1997, pp. 66–76.

[4] I. Stojmenovic, "Position-based routing in ad hoc networks," *IEEE Communications Magazine*, vol. 40, no. 7, pp. 128–134, Aug. 2002.

[5] C. Maihofer, "A survey of geocast routing protocols," *IEEE Communications Surveys & Tutorials*, vol. 6, no. 2, pp. 32–42, Second Quarter 2004.

[6] C. A. Balanis, *Arrays: Linear, Planar, and Circular*, 3rd ed. Hoboken, New Jersey, USA: John Wiley & Sons, Inc., 2005.

[7] W.-Q. Wang, H. Shao, and J. Cai, "Range-angle-dependent beamforming by frequency diverse array antenna," *International journal of antennas and propagation*, vol. 2012, Aug. 2012.

[8] Y. Liu, H. Ruan, L. Wang, and A. Nehorai, "The random frequency diverse array: A new antenna structure for uncoupled direction-range indication in active sensing," *IEEE Journal of Selected Topics in Signal Processing*, vol. 11, no. 2, pp. 295–308, Mar. 2017.

[9] W. Khan, I. M. Qureshi, and S. Saeed, "Frequency diverse array radar with logarithmically increasing frequency offset," *IEEE Antennas and Wireless Propagation Letters*, vol. 14, pp. 499–502, Nov. 2015.

[10] A. Basit, I. M. Qureshi, W. Khan, S. u. Rehman, and M. M. Khan, "Beam pattern synthesis for an fda radar with hamming window-based nonuniform frequency offset," *IEEE Antennas and Wireless Propagation Letters*, vol. 16, pp. 2283–2286, Jun. 2017.

[11] A. Babakhani, D. B. Rutledge, and A. Hajimiri, "Transmitter architectures based on near-field direct antenna modulation," *IEEE Journal of Solid-State Circuits*, vol. 43, no. 12, pp. 2674–2692, Dec. 2008.

[12] M. P. Daly and J. T. Bernhard, "Beamsteering in pattern reconfigurable arrays using directional modulation," *IEEE Transactions on Antennas and Propagation*, vol. 58, no. 7, pp. 2259–2265, Jul. 2010.

[13] ——, "Directional modulation technique for phased arrays," *IEEE Transactions on Antennas and Propagation*, vol. 57, no. 9, pp. 2633–2640, Sep. 2009.

[14] Y. Ding and V. Fusco, "Orthogonal vector approach for synthesis of multi-beam directional modulation transmitters," *IEEE Antennas and Wireless Propagation Letters*, vol. 14, pp. 1330–1333, Feb. 2015.

[15] H. Aggrawal, R. Puhl, and A. Babakhani, "Ultra-wideband pulse-based directional modulation," in *2015 IEEE MTT-S International Microwave and RF Conference (IMaRC)*, Dec. 2015, pp. 292–295.

[16] B. Qiu, J. Xie, L. Wang, and Y. Wang, "Artificial-noise-aided secure transmission for proximal legitimate user and eavesdropper based on frequency diverse arrays," *IEEE Access*, vol. 6, pp. 52 531–52 543, Sep. 2018.

[17] J. Hu, S. Yan, F. Shu, J. Wang, J. Li, and Y. Zhang, "Artificial-noise-aided secure transmission with directional modulation based on random frequency diverse arrays," *IEEE Access*, vol. 5, pp. 1658–1667, Jan. 2017.

[18] F. Shu, X. Wu, J. Hu, J. Li, R. Chen, and J. Wang, "Secure and precise wireless transmission for random-subcarrier-selection-based directional modulation transmit antenna array," *IEEE Journal on Selected Areas in Communications*, vol. 36, no. 4, pp. 890–904, Apr. 2018.

[19] S. Wang, S. Yan, J. Zhang, N. Yang, R. Chen, and F. Shu, "Secrecy zone achieved by directional modulation with random frequency diverse array," *IEEE Transactions on Vehicular Technology*, vol. 70, no. 2, pp. 2001–2006, Jan. 2021.

[20] F. Shu, L. Xu, J. Wang, W. Zhu, and Z. Xiaobo, "Artificial-noise-aided secure multicast precoding for directional modulation systems," *IEEE Transactions on Vehicular Technology*, vol. 67, no. 7, pp. 6658–6662, Jan. 2018.

[21] B. Qiu, M. Tao, L. Wang, J. Xie, and Y. Wang, "Multi-beam directional modulation synthesis scheme based on frequency diverse array," *IEEE Transactions on Information Forensics and Security*, vol. 14, no. 10, pp. 2593–2606, Feb. 2019.

[22] J. Xie, B. Qiu, Q. Wang, and J. Qu, "Broadcasting directional modulation based on random frequency diverse array," *Wireless Communications and Mobile Computing*, vol. 2019, May 2019.

[23] Y. Ding, A. Narbudowicz, and G. Goussetis, "Physical limitation of range-domain secrecy using frequency diverse arrays," *IEEE Access*, vol. 8, pp. 63 302–63 309, Mar. 2020.

[24] J. Sarrazin, M. Odhiambo, S. Golstein, P. De Doncker, and F. Horlin, "Spatial data focusing: An alternative to beamforming for geocasting scenarios," in *2018 USNC-URSI Radio Science Meeting (Joint with AP-S Symposium)*, Boston, MA, USA, Jul. 2018, pp. 139–140.

[25] G. Molineaux, S. Golstein, M. Odhiambo, F. Horlin, P. De Doncker, and J. Sarrazin, "Spatial data focusing using time and iq resources for wireless geocasting," in *2019 IEEE Global Communications Conference (GLOBECOM)*, Waikoloa, HI, USA, Dec. 2019, pp. 1–6.

[26] S. Ke, M. He, X. Bu, and W. Cai, "A leakage-based directional modulation scheme for frequency diverse array in robot swarm networks," *IEEE Access*, vol. 8, pp. 107 823–107 837, Jun. 2020.

[27] G. Molineaux, M. Odhiambo, F. Horlin, P. De Doncker, and J. Sarrazin, "Ofdm-based spatial data focusing for high resolution 2-dimensional wireless geocasting," in *2020 IEEE 31st Annual International Symposium on Personal, Indoor and Mobile Radio Communications*, London, United Kingdom (Great Britain), Aug. 2020, pp. 1–6.

[28] R. Gallager, "Low-density parity-check codes," *IRE Transactions on Information Theory*, vol. 8, no. 1, pp. 21–28, Jan. 1962.

[29] M. Ester, H.-P. Kriegel, J. Sander, and X. Xu, "A density-based algorithm for discovering clusters in large spatial databases with noise," in *Proceedings of the Second International Conference on Knowledge*

Discovery and Data Mining (KDD-96), vol. 96, no. 34, Portland, OR, USA, Aug. 1996, pp. 226–231.

[30] S. K. Yoo, S. L. Cotton, R. W. Heath, and Y. J. Chun, "Measurements of the 60 GHz ue to enb channel for small cell deployments," *IEEE Wireless Communications Letters*, vol. 6, no. 2, pp. 178–181, Apr. 2017.

[31] M. Shafi, J. Zhang, H. Tataria, A. F. Molisch, S. Sun, T. S. Rappaport, F. Tufvesson, S. Wu, and K. Kitao, "Microwave vs. millimeter-wave propagation channels: Key differences and impact on 5G cellular systems," *IEEE Communications Magazine*, vol. 56, no. 12, pp. 14–20, Dec. 2018.

Philippe De Doncker received the M.Sc. degree in Physics Engineering and the Ph.D. degree in science engineering from the Université libre de Bruxelles (ULB), Brussels, Belgium, in 1996 and 2001, respectively. He founded the Wireless Communications Group in 2007. He is currently a Full Professor with ULB, and leads the research activities on wireless channel modeling and electromagnetics.

Guylian Molineaux received the M.Sc. degree in Electrical Engineering from the Vrije Universiteit Brussel (VUB), Belgium, in 2019. Since October 2019, he is a FRIA Ph.D. Fellow of the F.R.S.-FNRS, working in the Wireless Communications Group of Université Libre de Bruxelles (ULB), Belgium, and the Group of Electrical Engineering of Paris (GeePs) at Sorbonne Université, France. His research is based around wireless physical layer geocasting, using Spatial Data Focusing.

François Horlin received the Ph.D. degree from the Université catholique de Louvain (UCL) in 2002. He specialized in the field of signal processing for digital communications. His Ph.D. research aimed at optimizing the multi-access for 3G cellular communications. He joined the Inter-university Micro-Electronics Center (IMEC) in 2006 as a senior scientist. He worked on the design efficient transceivers that can cope with the channel and hardware impairments in the context of 4G cellular systems. In 2007, François Horlin became professor at the Université libre de Bruxelles (ULB). He is supervising a research team working on modern communication, localisation and passive radar systems.

Julien Sarrazin received his Engineering diploma/Master of Research, and Ph.D. degrees from the University of Nantes in France, in 2005 and 2008 respectively. In 2009 and 2010, he worked at the BK Birla Institute of Technology of Pilani, in India, where he was in charge of telecommunication-related teaching. In 2011 and 2012, he was a research engineer at Telecom ParisTech in Paris. Since September 2012, he is an Associate Professor at Sorbonne Université (formerly University of Pierre and Marie Curie) in Paris, where he is currently working in the GeePs research institute (Group of Electrical Engineering of Paris) in the field of Spatial Data Focusing, antenna design, and localization. His research interests also include channel modeling and physical layer security.